

Supporting information

Negative Area Compressibility of a Hydrogen-Bonded Two-Dimensional Material

Guoqiang Feng,^{b, a, c} Wei-Xiong Zhang,^d Liyuan Dong,^c Wei Li,^{*, a, c} Weizhao Cai,^{*, e}

Wenjuan Wei,^c Lijun Ji,^c Zheshuai Lin,^{*, f} Peixiang Lu^{*, c, g}

^a*School of Materials Science and Engineering, Nankai University, Tianjin 300350, China. E-mail: w1276@nankai.edu.cn*

^b*Department of Physics and Mechanical & Electrical Engineering, Hubei University of Education, Wuhan 430205, China*

^c*School of Physics, Huazhong University of Science and Technology, Wuhan 430074, China*

^d*School of Chemistry and Chemical Engineering, Sun Yat-Sen University, Guangzhou 510275, China*

^e*Department of Physics and Astronomy, University of Utah, Salt Lake City, Utah 84112, United States. E-mail: wzhcai@gmail.com*

^f*Center for Crystal R&D, Key Lab of Functional Crystals and Laser Technology of Chinese Academy of Sciences, Technical Institute of Physics and Chemistry, Chinese Academy of Sciences, Beijing 100190, China. E-mail: zslin@mail.ipc.ac.cn*

^g*Laboratory for Optical Information Technology, Wuhan Institute of Technology, Wuhan 430205, China. E-mail: lupeixiang@hust.edu.cn*

Nanoindentation experimental analysis

Nanoindentation experiments were conducted using a Berkovich tip with a radius of ~50 nm in quasi-static mode. In order to identify flat regions for the experiment, the crystal surfaces were imaged prior to indentation using the same indenter tip. A loading and unloading rate of 0.5 mN/s and a hold time of 10 s at peak load were employed. A minimum of 10-15 indentations were performed on each crystallographic facets (Fig. S2). The indentation impressions were captured immediately after unloading, so as to avoid time-dependent elastic recovery of the residual impression. Young's modulus (E) and hardness (H) of the $\text{Zn}(\text{CH}_3\text{COO})_2 \bullet 2\text{H}_2\text{O}$ crystals were determined *via* the standard Oliver-Pharr Method.¹ The load-indentation depth ($P-h$) curves are displayed in Fig. S2. Several features are noteworthy. (1) The resistance to the penetration of the indenter is slightly higher on (001) than on (100). (100) exhibits a higher indentation depth in comparison to (001) signifying that plastic flow occurs more readily when the (100) face of the crystal is indented. This difference in the elastic response is due to arrangement of layer-stacking structure. And the $P-h$ curve shows relative small residual depths upon unloading, which implies that elastic recovery occurs during unloading. The large elastic recovery (50%) on (100) face of crystal $\text{Zn}(\text{CH}_3\text{COO})_2 \bullet 2\text{H}_2\text{O}$ is much higher than the elastic recovery for (100) of saccharin (9%),² (100) of aspirin (35%),³ and (101) of sodium saccharinate (25%).⁴ (2) On the two $P-h$ curves of $\text{Zn}(\text{CH}_3\text{COO})_2 \bullet 2\text{H}_2\text{O}$, several discrete displacement bursts ('pop-ins') in the loading portion indicate that the plastic deformation occurs intermittently (Fig. S2c). For the (100) face, the first significant displacement burst occurs at 0.14 mN with a magnitude of about 12 nm ($h_{\text{pop-in}}$), the subsequently pop-ins with $h_{\text{pop-in}}$ are 5, 3.5, 13, 6.3, 2.8, 0.6, 22, 2.8 nm. These pop-ins are close to the integral multiple of $d_{(100)}$ (7.090 Å). On the curve of (001), the first significant displacement of 4 nm is observed to occur at 0.195 N, the subsequently displacement are 10, 4, 3.7, 2.8, 3.5, 4, 18, 5, 2.2 nm, which are approximately an integral multiple of the interplanar spacing of (001) with a distance of 5.399 Å. Such a correspondence between a pop-in magnitude and interplanar spacing is discovered in saccharin, aspirin and sodium saccharinate. These observations allow for the possible explanation of plastic deformation attributed to slipping along a crystallographic plane in layered crystals and relaxation of the sudden indenting-imposed stress. (3) As shown in Fig. S2, the crystal $\text{Zn}(\text{CH}_3\text{COO})_2 \bullet 2\text{H}_2\text{O}$ features elasticity and plasticity. During indentation, crystal either stretch apart (elastic deformation) or slide relative to each other (plastic deformation). The average values of E and H values are 4.3(2) and 0.37(2) GPa for (100), and 5.8(3) and 0.58(5) GPa for (001), respectively. The modulus shows medium anisotropy with $E_{(001)} / E_{(100)} = 1.35/1$ in elastic deformation, while the hardness exhibits large anisotropy with $H_{(001)} / H_{(100)} = 1.57/1$ in plastic deformation. Further, the difference (26%) in the moduli for the crystal faces indicates possible dissimilarities in the interaction features. And the much larger anisotropy in H (36%) suggests significant differences in the micro-mechanisms of plasticity.⁵ Therefore, the H and E values obtained on the two different natural facets for the (100) and (001) faces manifest significant mechanical anisotropy of $\text{Zn}(\text{CH}_3\text{COO})_2 \bullet 2\text{H}_2\text{O}$.

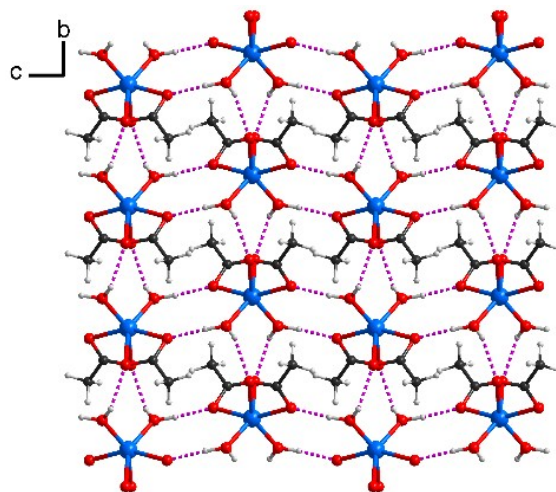


Fig. S1 Interactions of an individual layer in $\text{Zn}(\text{CH}_3\text{COO})_2 \bullet 2\text{H}_2\text{O}$.⁶ Colour scheme: Zn^{2+} , blue; O, red; C, black; H, white; the purple dotted lines represent the $\text{O}-\text{H}\cdots\text{O}$ hydrogen bonds.

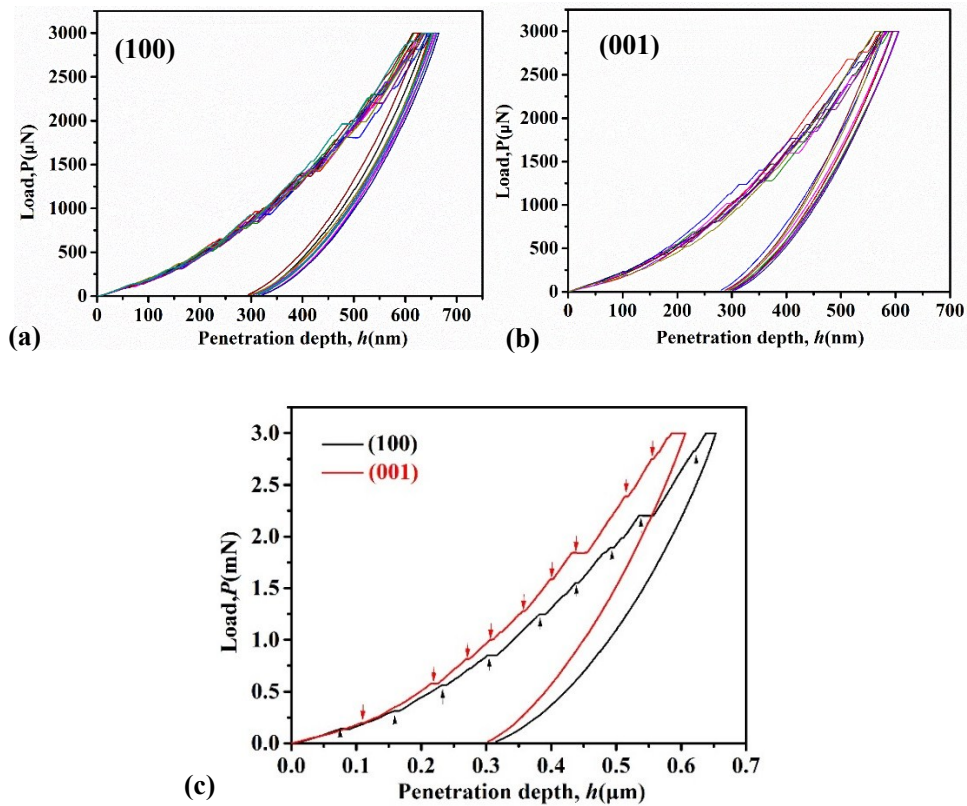


Fig. S2 (a) and (b) Load-displacement ($P-h$) curves obtained normal to the (001) and (100) faces of $\text{Zn}(\text{CH}_3\text{COO})_2 \bullet 2\text{H}_2\text{O}$ using a Berkovich indenter. (c) Representative $P-h$ curves obtained from indentation on the (001) and (100) faces of $\text{Zn}(\text{CH}_3\text{COO})_2 \bullet 2\text{H}_2\text{O}$ showing characteristic ‘pop-ins’.

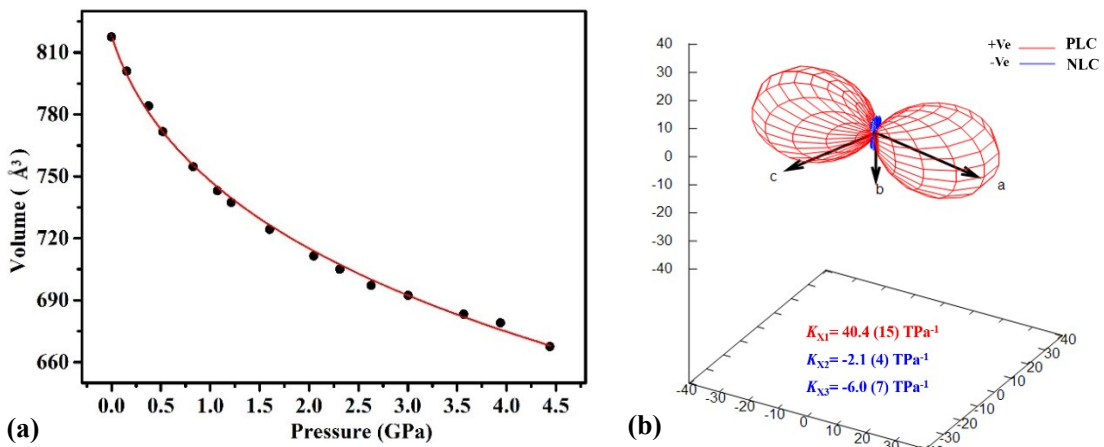


Fig. S3 (a) The evolution of unit cell volume as a function of pressure. The experimental data are shown, with error bars, as black dots, and the red line represents the third-order Birch-Murnaghan fits obtained using EosFit7.⁷ The $V(P)$ data for $\text{Zn}(\text{CH}_3\text{COO})_2 \cdot 2\text{H}_2\text{O}$ was fitted with third-order Birch-Murnaghan equation of state which yields the isothermal bulk modulus of $20(2)$ GPa; (b)The experimental compressibility indicatrix in the range of ambient–4.44 GPa. In the blank, the magnitudes of the corresponding compressibility K_{X1} , K_{X2} and K_{X3} are listed. The blue values correspond to negative linear compressibility (NLC) and the red ones to positive linear compressibility (PLC).

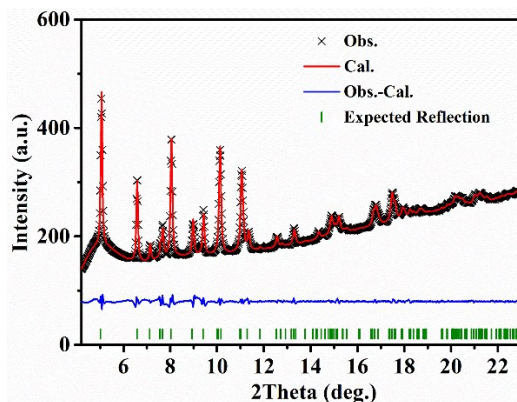


Fig. S4 The synchrotron powder X-ray diffraction spectra of $\text{Zn}(\text{CH}_3\text{COO})_2 \cdot 2\text{H}_2\text{O}$ refined using the Pawley method at ambient conditions. The black, red symbol and blue continuous line are experimental, calculated and difference profiles, respectively, and the vertical markers indicate the allowed Bragg reflections in the space group of $C2/c$.

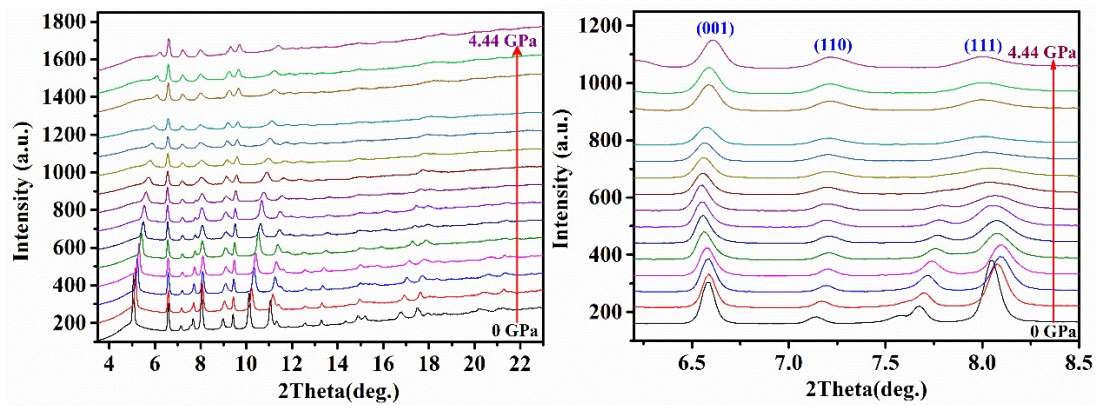


Fig. S5 Recorded patterns of the HP-XRD for $\text{Zn}(\text{CH}_3\text{COO})_2 \bullet 2\text{H}_2\text{O}$ displayed in the left panel, while the Bragg peaks of (001), (110) and (111) are enhanced in the right panel.

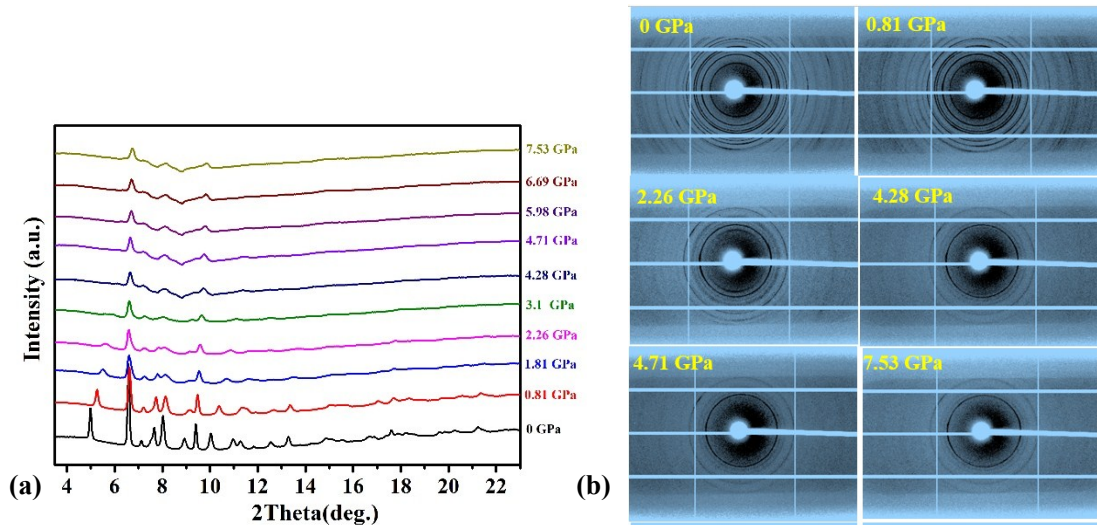


Fig. S6 (a) The HP-XRD patterns of $\text{Zn}(\text{CH}_3\text{COO})_2 \bullet 2\text{H}_2\text{O}$, collected in the second series of measurements from ambient -7.53 GPa; (b) Representative 2D XRD images at specific pressures.

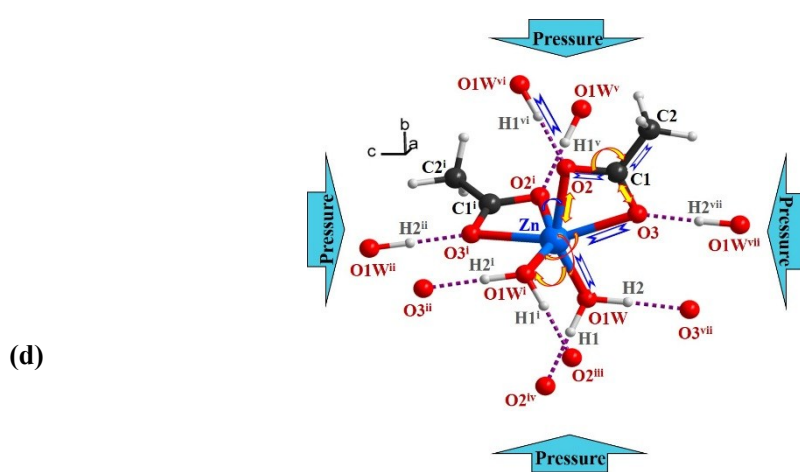
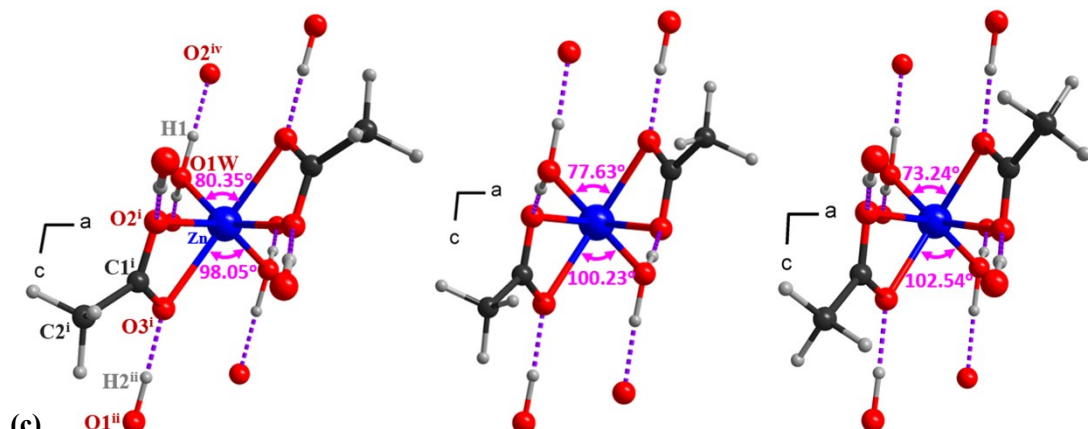
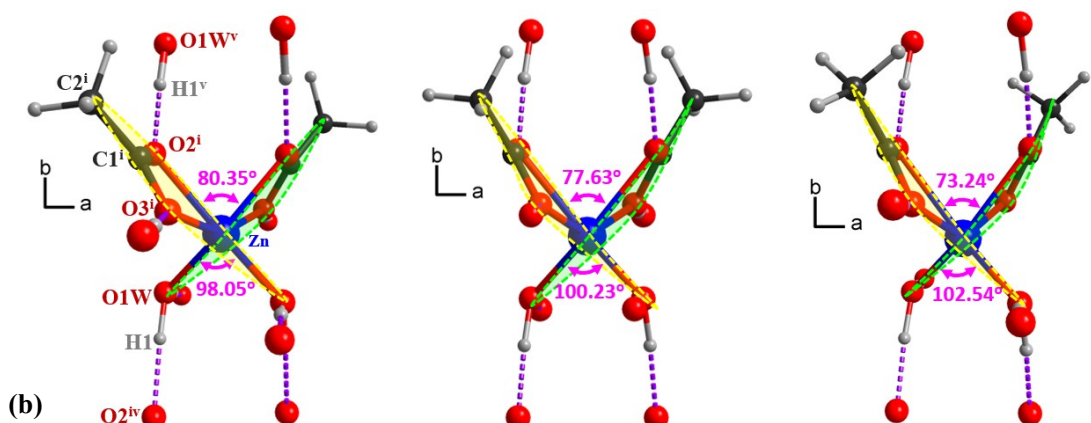
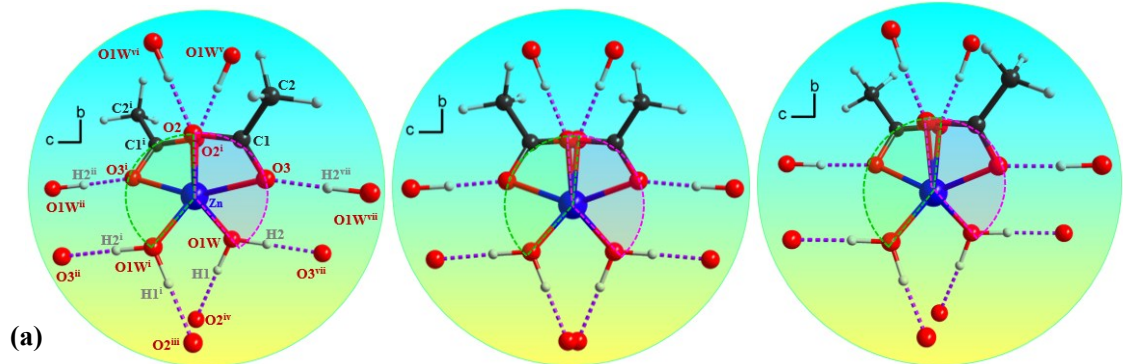


Fig. S7 The conformation of the coordination geometry viewed along *a*- (a) *c*- (b) and *b*-axis (c), at ambient, 2.05 and 4.44 GPa, calculated from DFT based on experiment cell parameters. Note: the intersectional angle O2-Zn-O2ⁱ concurrently decreases from 80.35°, 77.63° to 73.24°, accompanied by the increase of the O1W-Zn-O1Wⁱ angle from 98.05°, 100.23° to 102.54°, at ambient, 2.05 and 4.44 GPa. (d) Trend in variations of the bonding lengths and angles of the Zn(CH₃COO)₂•2H₂O structure. The blue and yellow double-headed arrows indicate the contraction of bonds (C1–O2, C1–C2, O1W^{vi}–H1^{vi}···O2, O3–Zn and O1W–Zn) and stretch of bonds (C1–O2 and O2–Zn), respectively. The blue and yellow single-headed arrows indicate shrinkage of angles (\angle O2–Zn–O2ⁱ) and increase of angles (\angle O2–C1–C2, O1W–Zn–O1Wⁱ, O3–Zn–O1Wⁱ and O1W–Zn–O2), respectively, with the increase of hydrostatic pressure. Symmetry codes: (i) -*x*, *y*, 0.5–*z*; (ii) *x*, -*y*, 0.5+*z*; (iii) *x*, -1+*y*, *z*; (iv) -*x*, -1+*y*, 0.5–*z*; (v) *x*, 1+*y*, *z*; (vi) -*x*, 1+*y*, 0.5–*z*; (vii) -*x*, -*y*, -*z*.

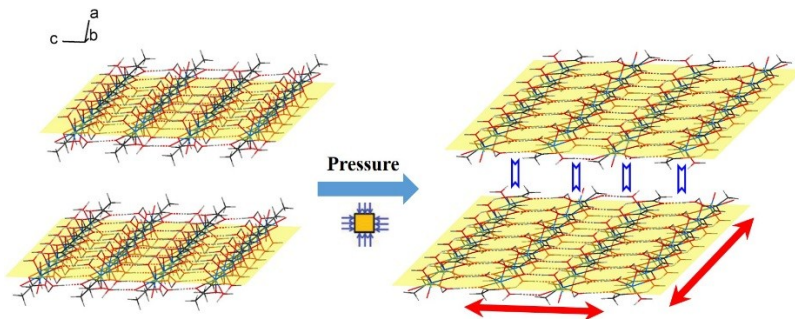


Fig. S8 The generic mechanical response of the layer crystal links the expansion of **X3** and **X2** direction to the opposite rotating of two ‘fan-shaped’ structures and distortion of acetate ligands, and the shrink of **X1** direction in association with weak van der Waals interactions under hydrostatic compression. Note: the **X1** principal axis is approximately along the *a*-axis, the **X2** principal axis is approximately oppositely along the *c*-axis, and the **X3** principal axis is oppositely along the *b*-axis (Table S2).

Table S1 The lattice parameters of $\text{Zn}(\text{CH}_3\text{COO})_2 \bullet 2\text{H}_2\text{O}$ from high-pressure synchrotron powder XRD experiments under different hydrostatic pressures from ambient to 4.44 GPa. The errors are given in the parentheses.

Pressure(GPa)	<i>a</i> (Å)	<i>b</i> (Å)	<i>c</i> (Å)	<i>θ</i> (deg)	<i>V</i> (Å ³)
0.0001	14.2488(15)	5.3182(7)	10.9532(14)	100.016(7)	817.5(3)
0.15	14.0087(24)	5.3050(9)	10.9428(28)	100.046(9)	800.9(4)
0.38	13.7486(26)	5.2948(9)	10.9309(21)	99.875(9)	784.1(5)
0.52	13.5373(29)	5.2929(11)	10.9154(24)	99.453(11)	771.6(5)
0.73	13.2121(34)	5.3032(12)	10.8846(30)	98.326(15)	754.7(6)
0.97	12.9973(46)	5.3058(17)	10.8730(40)	97.716(19)	743.1(8)
1.21	12.8724(51)	5.3119(16)	10.8728(43)	97.342(21)	737.4(8)
1.60	12.6325(41)	5.3263(16)	10.8337(32)	96.516(19)	724.3(7)
2.05	12.3817(50)	5.3391(20)	10.8137(48)	95.720(23)	711.4(9)
2.31	12.2524(58)	5.3453(22)	10.8139(51)	95.479(26)	705.0(10)
2.63	12.0704(52)	5.3697(20)	10.7933(48)	94.734(26)	697.2(9)
3.01	11.9085(49)	5.3994(21)	10.7945(47)	94.147(23)	692.3(9)
3.57	11.6980(40)	5.4227(17)	10.7918(38)	93.600(16)	683.3(7)
3.94	11.6687(36)	5.4138(16)	10.7700(33)	93.545(17)	679.1(6)
4.44	11.4333(40)	5.4390(17)	10.7484(36)	92.925(18)	667.6(7)

Table S2 Principal compressibilities and corresponding principal axes were determined using the PASCal software⁸ for $\text{Zn}(\text{CH}_3\text{COO})_2 \bullet 2\text{H}_2\text{O}$.

Principal axis, <i>i</i>	<i>K_{Xi}</i> (TPa ⁻¹)	Component of <i>Xi</i> along the crystallographic axes			Approximate axis
		<i>a</i>	<i>b</i>	<i>c</i>	
1	40.4(15)	0.9677	0	-0.2521	[100]
2	-2.1(4)	-0.2712	0	-0.9625	[00-1]
3	-6.0(7)	0	-1	0	[0-10]

Table S3 The experimental results of compressibility K_{x1} , K_{x2} and K_{x3} as a function of pressure from ambient to 4.44 GPa. The errors are given in the parentheses.

Pressure (GPa)	Compressibility (TPa ⁻¹)		
	K_{x1}	K_{x2}	K_{x3}
0.0001	--	--	--
0.15	115.45(20.64)	-1.54(2.01)	-1.32(3.85)
0.38	80.35(8.99)	-1.72(1.66)	-2.23(1.60)
0.52	70.44(6.21)	-1.8(1.48)	-2.7(1.13)
0.73	61.48(3.97)	-1.88(1.23)	-3.29(0.91)
0.97	54.6(2.51)	-1.95(0.98)	-3.91(0.90)
1.21	49.96(1.76)	-2(0.78)	-4.44(0.90)
1.60	44.6(1.36)	-2.07(0.53)	-5.23(0.83)
2.05	40.38(1.52)	-2.14(0.42)	-6.04(0.67)
2.31	38.44(1.69)	-2.17(0.45)	-6.49(0.57)
2.63	36.49(1.88)	-2.21(0.55)	-7(0.54)
3.01	34.56(2.08)	-2.25(0.70)	-7.57(0.67)
3.57	32.24(2.31)	-2.3(0.94)	-8.37(1.1)
3.94	30.96(2.44)	-2.33(1.09)	-8.87(1.47)
4.44	29.49(2.58)	-2.36(1.29)	-9.52(2.00)

Table S4 Selected bond lengths and angles of $\text{Zn}(\text{CH}_3\text{COO})_2 \bullet 2\text{H}_2\text{O}$ over the pressure range of ambient–4.44 GPa, calculated *via* DFT using experimental cell parameters. Symmetry codes: (i) -x, y, 0.5-z; (ii) x, -y, 0.5+z; (iii) x, -1+y, z; (iv) -x, -1+y, 0.5-z; (v) x, 1+y, z; (vi) -x, 1+y, 0.5-z; (vii) -x, -y, -z.

Pressure (GPa)	C1-C2 (Å)	C1-O2 (Å)	C1-O3 (Å)	Zn-O1W (Å)	Zn-O2 (Å)	Zn-O3 (Å)	O1W ^{vi} -H1 ^{vi} -O2 (Å)	O1W ^{vii} -H2 ^{vii} -O3 (Å)
0.0001	1.477	1.278	1.272	1.971	2.128	2.285	2.638	2.608
0.73	1.473	1.277	1.273	1.965	2.147	2.231	2.6	2.606
1.21	1.472	1.276	1.275	1.957	2.163	2.203	2.598	2.589
1.60	1.470	1.275	1.276	1.957	2.182	2.181	2.583	2.598
2.05	1.470	1.274	1.277	1.950	2.203	2.163	2.586	2.589
2.63	1.469	1.272	1.278	1.951	2.228	2.139	2.574	2.598
3.01	1.469	1.271	1.279	1.951	2.249	2.126	2.576	2.606
3.57	1.468	1.271	1.279	1.954	2.259	2.126	2.571	2.612
3.94	1.467	1.271	1.279	1.948	2.271	2.111	2.568	2.611
4.44	1.469	1.267	1.282	1.945	2.312	2.099	2.559	2.619

Pressure (GPa)	\angle O2-Zn-O2 ⁱ (°)	\angle O1W-Zn- O1W ⁱ (°)	\angle O1W-Zn- O2 (°)	\angle O1W ⁱ -Zn- O3 (°)	\angle C2-C1-O2 (°)	\angle C1-O3-O1W ^{vii} (°)	\angle O3 ^{vii} -O1W- O2 ^{iv} (°)
0.0001	80.35	98.05	147.85	105.99	120.14	119.68	107.21
0.73	79.53	99.11	148.89	107.98	120.10	119.27	107.25
1.21	78.86	98.56	148.23	109.67	120.22	119.68	107.70
1.60	77.99	99.79	149.36	110.52	120.33	118.78	107.98
2.05	77.63	100.23	149.20	111.58	120.52	118.55	108.46
2.63	76.21	100.61	149.74	112.72	120.53	117.55	109.37
3.01	75.47	100.74	149.85	113.43	120.60	117.08	109.87
3.57	74.61	100.69	150.31	113.73	120.63	116.68	110.52
3.94	74.62	101.47	150.05	113.73	120.61	116.30	110.36
4.44	73.24	102.54	149.83	113.49	121.82	114.12	112.30

Pressure (GPa)	\angle Zn-O2- H1 ^{vi} (°)	\angle C1-O2- H1 ^{vi} (°)	\angle O1W ^{vi} - H1 ^{vi} ...O2 (Å)	\angle O1W ^{vii} - H2 ^{vii} ...O3 (°)	\angle Zn-O1W- O3 ^{vii} (°)	\angle Zn-O3- O1W ^{vii} (°)
0.0001	129.09	120.70	177.54	178.32	118.32	151.78
0.73	130.68	118.27	176.81	177.79	118.83	150.88
1.21	130.00	118.84	177.05	177.68	121.64	149.06
1.60	131.90	116.78	176.46	177.49	120.13	149.47
2.05	131.79	116.29	176.74	177.37	121.13	148.62
2.63	133.26	115.52	176.08	177.54	120.64	148.42
3.01	133.72	115.27	175.98	177.60	120.83	148.02
3.57	134.94	114.64	174.94	178.33	120.21	147.94
3.94	134.59	114.96	175.70	177.77	120.57	147.81
4.44	135.10	116.64	175.02	177.99	119.66	147.95

References:

- (1) (a) W. C. Oliver, G. M. Pharr, *J. Mater. Res.* 1992, **7**, 1564–1583. (b) W. C. Oliver, G. M. Pharr, *J. Mater. Res.*, 2004, **19**, 3–20.
- (2) M. S. R. N. Kiran,; S. Varughese, C. M. Reddy, U. Ramamurty, G. R. Desiraju, *Cryst. Growth Des.*, 2010, **10**, 4650.
- (3) S. Varughese, M. S. R. N. Kiran, K. A. Solanko, A. D. Bond, U. Ramamurty, G. R. Desiraju, *Chem. Sci.*, 2011, **2**, 2236.
- (4) M. S. R. N. Kiran, S. Varughese, U. Ramamurty, G. R. Desiraju, *CrystEngComm.*, 2012, **14**, 2489.
- (5) S. Varughese, M. S. R. N. Kiran, U. Ramamurty, G. R. Desiraju, *Chem. Asian J.*, 2012, **7**, 2118.
- (6) T. Ishioka, A. Murata, Y. Kitagawa, K. T. Nakamura, *Acta Cryst.*, 1997, **C53**, 1029.
- (7) R. J. Angel, J. Gonzalez-Platas, M. Alvaro, *Z. Kristallogr.*, 2014, **229(5)**, 405.
- (8) M. J. Cliffe, A. L. Goodwin, *J. Appl. Cryst.*, 2012, **45**, 1321.